Physics in Medicine & Biology

LETTER • OPEN ACCESS

Versatile vasculature chips for ultrasound localization microscopy

To cite this article: Renxian Wang *et al* 2025 *Phys. Med. Biol.* **70** 21LT01

IOP Publishing Phys. Med. Biol. 70 (2025) 21LT01 https://doi.org/10.1088/1361-6560/ae11f6

Physics in Medicine & Biology

IPEM Institute of Physics and Engineering in Medicine

LETTER

Versatile vasculature chips for ultrasound localization microscopy

Renxian Wang[1], **Qi Liu**[2], **Xin Zhao**[2] and **Wei-Ning Lee**[1,3,*]

[1] Department of Electrical and Electronic Engineering, The University of Hong Kong, Hong Kong Special Administrative Region of China, People's Republic of China
[2] Department of Applied Biology and Chemical Technology, The Hong Kong Polytechnic University, Hong Kong Special Administrative Region of China, People's Republic of China
[3] School of Biomedical Engineering, The University of Hong Kong, Hong Kong Special Administrative Region of China, People's Republic of China
* Author to whom any correspondence should be addressed.

E-mail: wnlee@hku.hk

Keywords: microbubble, organ-on-a-chip, super-resolution imaging, ultrasound, microvasculature

Supplementary material for this article is available online

OPEN ACCESS

RECEIVED
17 June 2025

REVISED
26 September 2025

ACCEPTED FOR PUBLICATION
10 October 2025

PUBLISHED
17 October 2025

Abstract

Objective. Ultrasound localization microscopy (ULM) has revolutionized microvasculature imaging by surpassing the diffraction limit via microbubbles. While ULM demonstrates exceptional potential to resolve micron-scale vascular structures in both preclinical and clinical studies, its performance evaluation remains challenging primarily due to the lack of reference microvascular phantoms featuring realistic, micron-scale, and hierarchical vascular structures. This study thus aims to develop a fabrication protocol for microvasculature patterns that offers design versatility and enables on-demand customization. *Approach.* Inspired by microfluidic chip techniques, we present an organ-on-a-chip protocol for fabricating agarose-based micro-vessel network phantoms with ground truth. We experimentally demonstrated the feasibility of the vasculature phantom using two adapted patterns: (1) a leaf pattern, which exhibited intrinsic quasi-two-dimensional venation network with hierarchical and branching channels similar to animal vasculature, and (2) a kidney pattern derived from a two-dimensional projection of real human vasculature obtained via micro computed tomography. Microbubble solutions were perfused into the phantoms by capillary force and gravity. *Main results.* The ULM-reconstructed vasculature maps agreed well with the ground truth. ULM achieved high sensitivity values of 0.97 and 0.95, but low precision values of 0.37 and 0.60, for the leaf and kidney phantom, respectively. The results indicated the capability of ULM to reconstruct vessel structures while making many false positive predictions. *Significance.* The proposed protocol provides a versatile platform for creating realistic microvascular phantoms, facilitating the development, evaluation, and optimization of ultrasound microvascular imaging techniques.

1. Introduction

Ultrasound localization microscopy (ULM) is an acoustic super-resolution imaging technique for mapping microcirculation in a living body with the help of gas-filled microbubbles (MBs) that are injected and flow in the circulatory system (Errico *et al* 2015). Through precise localization and tracking of individual micron-level MBs, ULM overcomes the acoustic diffraction limit and achieves unprecedented micrometric resolution for deep tissue imaging *in vivo*, closing the gap across various imaging modalities (Christensen-Jeffries *et al* 2020). ULM has shown great potential for broad clinical applicability across various biological tissues, including the brain (Demene *et al* 2021, Heiles *et al* 2022, Lowerison *et al* 2022), kidney (Heiles *et al* 2022, Chabouh *et al* 2024), heart (Yan *et al* 2024), lymph node (Yan *et al* 2022), and so on. ULM is a multi-step framework, typically consisting of ultrasound data acquisitions

of serial frames, MB signal extraction from raw data, MB localization for subpixel accuracy and tracking, and then accumulation of sub-wavelength tracks for final vasculature. Researchers have been working for over ten years on improving the accuracy and efficiency of the ULM workflow, involving various localization and tracking algorithms (Song *et al* 2018, Heiles *et al* 2022, Yan *et al* 2022, Chen *et al* 2023, Lerendegui *et al* 2024).

However, validation of ULM remains a critical bottleneck due to the lack of realistic vasculature phantoms that serve as ground truth. The μm diameter, branching, and hierarchical nature of blood vessels makes it challenging to fabricate microvasculature phantoms for assessment of ULM-reconstructed results. The existing validation methods for ULM mainly rely on simulations, manually-assembled tube phantoms with simple geometries, and micro-CT (micro computed tomography). A research group used the Verasonics Research Ultrasound Simulator (Heiles *et al* 2022) to model each MB as a point scatterer with addictive white Gaussian noise. PROTEUS (Blanken *et al* 2024) is a recently developed simulator that incorporates flow dynamics for contrast-enhanced ultrasound imaging of realistic vascular structures. It is a customizable framework for ULM validation. A phantom with two crossed tubes of around 200 μm in diameter was commonly used for ULM validation (Zhang *et al* 2019, Riemer *et al* 2023, Wang *et al* 2024). Recently, one study (Parra Raad *et al* 2024) proposed to manually fabricate a hierarchical microvascular phantom with the diameter down to around $\lambda/6$ ($\lambda = \sim 350$ μm) based on polydimethylsiloxane (PDMS). Kawara *et al* (2023) fabricated capillary-scale hydrogel microchannel networks, realizing micron scale flow channels but simple branches. Gelatin-based microfluidic phantoms (Mano *et al* 2023, Gershman *et al* 2025) with a channel diameter of 100 μm were also proposed for ULM, but their structures remained rather simplified. Some studies (Andersen *et al* 2021, Hansen *et al* 2025) employed micro-CT to validate ultrasound microvascular imaging, but the spatial registration between the two imaging modalities is nontrivial. Overall, simulations can emulate customized and realistic microstructures but hardly replicate actual experimental data; existing phantoms generally do not incorporate micron-level sizes, hierarchical branches, and realistic vascular structures concurrently.

To address the aforementioned challenges, we propose an on-chip versatile vasculature phantom protocol for ultrasound microvascular imaging, inspired by a leaf-templated microfluidic chip technique (Mao *et al* 2018, 2020, Fang *et al* 2023, Ji *et al* 2023), with the initial application focused on ULM. We adapted microvasculature patterns as microfluidic channels with sizes of tens of microns and realistic hierarchical branching structures on an agarose layer. Customization of each microvascular structure served as a structural ground truth. In the following sections, we first introduce the protocol and then present experimental results, demonstrating its effectiveness and potential for the development and clinical adoption of ultrasound microvascular imaging techniques.

2. Methods

Our protocol follows the typical fabrication workflow of a microfluidic chip, incorporating customized vasculature patterns. As figure 1(a) shows, we binarized a photo of a target pattern provided by the public datasets (Walsh *et al* 2021, Li *et al* 2022) and converted it into a vectograph by AutoCAD 2022. The vectograph pattern was then transferred onto a chrome-coated photomask for photolithography on a silicon wafer to replicate the pattern. In brief, a photosensitive polymer was spin-coated onto the silicon wafer, solidified, and exposed to UV light through the photomask. The polymer in the UV-irradiated region was dissolved in a developer solution, and the designed pattern was then replicated on the silicon wafer. A 3% agarose solution was then cast onto the silicon mould. The agarose with the negative pattern of the target vasculature was peeled off from the silicon mould after approximately 10 min of solidification at 25 °C.

The protocol allows for versatile customization of the vascular network. In this study, we used two vascular patterns (figure 1(a)) adapted from a Chinese rose leaf (Li *et al* 2022) and a human kidney (Walsh *et al* 2021). The leaf venation comprised quasi-two-dimensional (2D), hierarchical, and branching channels with high similarity to animal vasculature. As shown in figures 1(b)–(d), the agarose layer with vasculature network was then tightly sealed to a flat agarose slab (3% agarose, thickness: ~6 mm) for MB perfusion and ultrasound imaging. The inlet and outlet were cut out to expose the stem channels of the vasculature network for better perfusion. The MB solution (2×10^7–3×10^7 MBs ml^{-1}, USphere^{TM}, Trust Bio-sonics, Hsinchu County, Taiwan) was administered at the inlet and driven by capillary force and gravity.

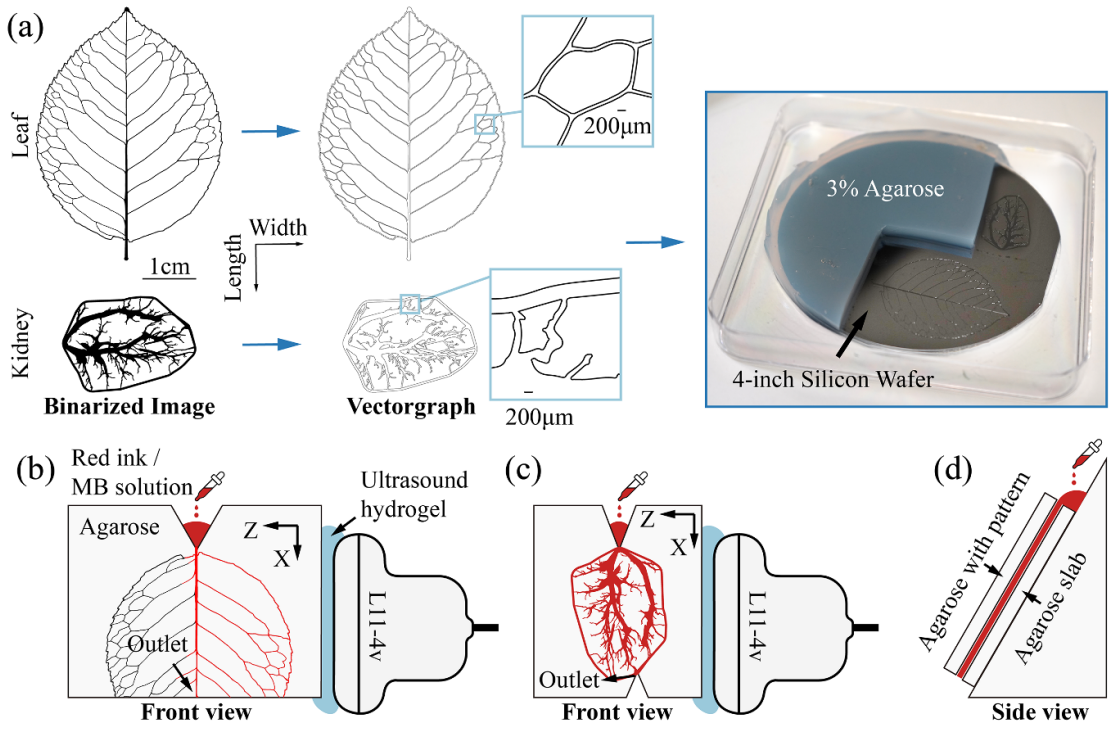

Figure 1. The proposed fabrication protocol of on-chip versatile vasculature phantoms for ultrasound microvascular imaging. (a) Vasculature photos were binarized and converted to vectographs for photolithography on a 4-inch silicon wafer. Micro-channels with the designed vasculature patterns were replicated from the silicon wafer. The leaf and kidney phantoms have physical dimensions (length × width × channel depth) of 47.2 mm × 34.8 mm × 240 μm and 18.4 mm × 25.6 mm × 240 μm, respectively. (b)–(d) The ultrasound imaging set-up for data acquisitions. (b) and (c) show the front view of the leaf and kidney phantoms, respectively, and (d) shows the side view. MB denotes microbubble. The red ink is to illustrate perfused vascular regions.

Ultrasound data were acquired at a compounded frame rate of 400 Hz with five tilted plane waves (-4; -2; 0; 2; 4°) using a linear probe L11-4v (6.25 MHz, 128 elements, pitch = 0.30 mm) connected to a Verasonics Vantage 256 system (Verasonics Inc, Kirkland, WA, USA). Each acquisition lasted for four seconds as a bloc, commencing immediately from the start of MB solution perfusion. The total number of blocs was 50 for the leaf phantom and 30 for the kidney phantom.

The PALA ULM workflow (Heiles *et al* 2022) was then adopted to reconstruct the vasculature network. It began with MB signal extraction by singular value decomposition (SVD). We then employed a Gaussian-fitting method for MB localization (Heiles *et al* 2022) and a Hungarian method (Kuhn 1955) for MB tracking. The ULM-derived vasculature was lastly compared with the corresponding ground truth obtained from its original AutoCAD design.

We considered the vessel ground truth from the designed pattern in the AutoCAD file as a binarized mask, with the vascular network region as the target. For quantitative comparison, ULM results (figures 2(b) and 3(d)) were first normalized by dividing each pixel value by the maximum pixel intensity in each selected ROI. The normalized ULM maps were then binarized using different empirical thresholds (*th*); pixels with intensities greater than *th* were assigned a value of 1 (positive), while all other pixels were assigned a value of 0 (negative). The ULM results were manually registered to ground truth. Positive pixels in the binarized ULM results that fell within the vascular region of the ground truth were regarded as true positives (TPs), while those in the non-vascular region were considered false positives (FPs). Negative pixels in the binarized ULM results that actually corresponded to the vascular region of the ground truth were labeled as false negatives (FNs). Precision, sensitivity, the Jaccard (JAC) index (Heiles *et al* 2022), and structural similarity index measure (SSIM) (Wang *et al* 2004) were computed for quantitative evaluation of the ULM results and respectively defined as

$$\text{Precision} = \frac{\text{TP}}{\text{TP} + \text{FP}} \tag{1}$$

$$\text{Sensitivity} = \frac{\text{TP}}{\text{TP} + \text{FN}} \tag{2}$$

$$\mathrm{JAC} = \frac{\mathrm{TP}}{\mathrm{TP} + \mathrm{FP} + \mathrm{FN}} \tag{3}$$

$$\mathrm{SSIM}(x, y) = \frac{\left(2\mu_x\mu_y + c_1\right)\left(2\sigma_{xy} + c_2\right)}{\left(\mu_x^2 + \mu_y^2 + c_1\right)\left(\sigma_x^2 + \sigma_y^2 + c_2\right)} \tag{4}$$

where x and y are the ULM map and ground truth image, respectively, μ and σ^2 denote the average and variance of pixel intensities, respectively, and σ_{xy} is the covariance of the ULM map and ground truth. c_1 (10^{-4}) and c_2 (9×10^{-4}) are small constants to avoid division by zero and stabilize the formula. Note that pixels with intensities greater than *th* were unchanged, while all other pixels were set to 0 (negative), for the SSIM metric.

3. Results

Figure 2(a) shows the ULM vasculature map of the leaf phantom, corresponding to a 90° counter-clockwise rotation of the imaging view shown in figure 1(b). The upper part of the leaf venation network was reconstructed well, but the rest was not. The light blue box in figure 2(a) was zoomed-in for better visualization (figure 2(b)) and binarized (figure 2(c)) with $th = 0$ for comparison with the ground truth (figure 2(d)). Figure 2(e) shows the cross-sectional vessel profiles along lines 1, 2, and 3 in figure 2(b) with measured diameters (69.0 μm, 51.5 μm, and 58.0 μm, respectively) around or below $\lambda/4$ ($\lambda = 246$ μm). The ULM-estimated diameters were about 45%–75% of the ground truth values. The peaks of the ULM intensity profiles were all located within the ground truth vessels.

A flow speed analysis of the leaf phantom was also performed. Figure 2(f) shows the flow speed map, and the region enclosed by the red box is magnified for visual comparison (figure 2(g)). Figure 2(h) shows the speed profiles across the channels indicated by lines 1, 2, and 3 in figure 2(g), whose ground truth widths were 196.3 μm, 154.9 μm, and 112.4 μm, respectively. The result confirmed a higher flow speed in a larger vessel (line 1). Figure 2(i) shows the proportion of the flow speed distribution in the flow speed map of the entire field of view in figure 2(f) and curve fitting (red line) by a log-normal distribution. The log-normal distribution was chosen as it was used to describe the flow velocities in lymph nodes (Jafarnejad *et al* 2019) and human heart vessels (Yan *et al* 2024). The mean flow speed in the leaf phantom was approximately 18 mm s^{-1}.

The kidney pattern was much more challenging to reconstruct because it has more hierarchical and branching structures. Yet, its ULM result (figure 3(a)) was in good qualitative agreement with the ground truth (figure 3(c)) despite some deviations in their details. The main branches were delineated well in the ULM map, while some complex microchannels were not reconstructed, particularly the cul-de-sac channels indicated by the turquoise triangles (figure 3). ULM also did not detect vessels in the positions of the purple triangles (figure 3). Some MBs flowed outside the micro-channels, and their flow paths were delineated as free trajectories (orange triangles in figure 3).

Figure 4(a) shows the quantitative analysis of the leaf ULM map enclosed by the light blue box (figure 2(b)), which exhibited complex network. Empirical thresholds (0, 0.01, 0.025, 0.05, 0.1, 0.2, 0.3) were applied to the leaf ULM result for binarization and subsequent evaluation. As the threshold increased, the precision increased from 0.37 to 0.84 while the sensitivity decreased from 0.97 to 0.27. The JAC index reached its maximum, approximately 0.51, at the threshold of 0.01. Figure 4(b) shows the quantitative analysis of the ULM result for the kidney phantom from the average of the three ROIs with branching structures in figure 3(d). The three ROIs corresponded to the three locations labeled in figure 3(c). The thresholds were selected empirically as 0, 0.005, 0.01, 0.02, 0.035, 0.05, and 0.1 for binarization on the three ROIs. As the threshold increased, the precision increased from 0.60 to 0.92, while the sensitivity dropped from 0.95 to 0.37. The JAC index initially increased to the maximum, approximately 0.70, when $th = 0.005$, and then decreased to 0.35 at $th = 0.1$. The SSIM values for the leaf and kidney phantoms were approximately 0.88 and 0.65, respectively, and remained consistent across different thresholds. Note that the aforementioned cul-de-sac regions were not included in the quantitative analysis of the three ROIs (marked by the yellow arrows in figure 3(d)).

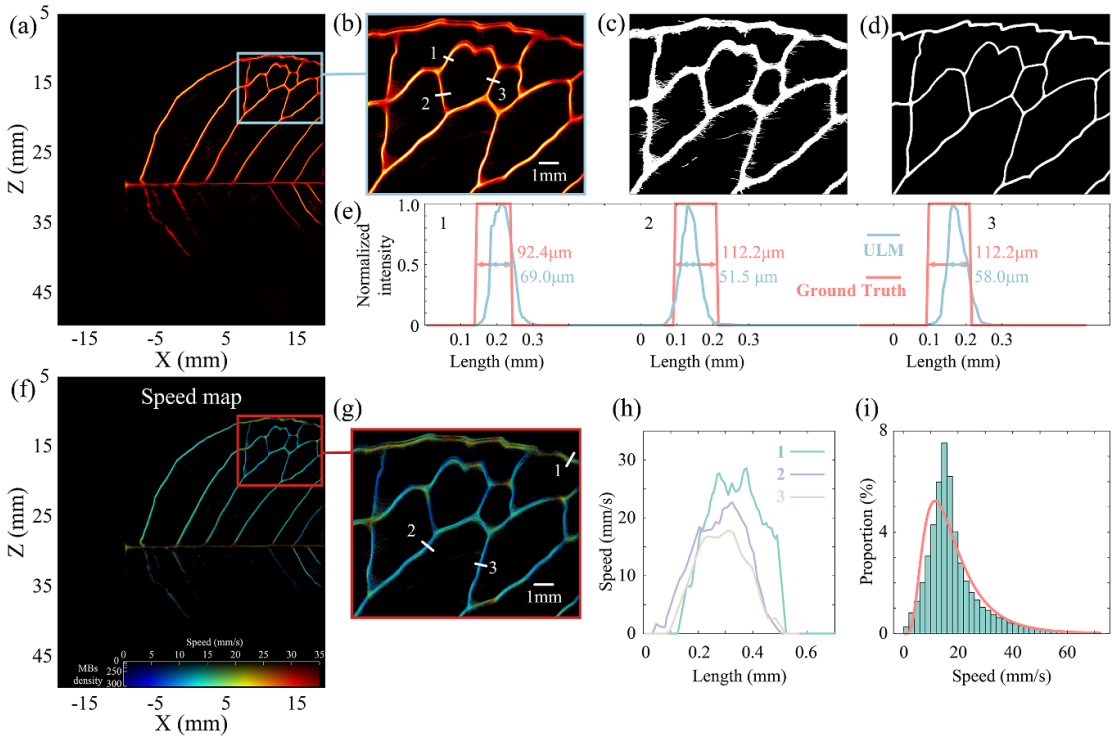

Figure 2. ULM of a leaf phantom: (a) The ULM density map of the leaf phantom in the front view (90° counterclockwise rotation of figure 1(b)). (b) Magnification of the venation network enclosed by the light blue box in (a). (c) Binarized vasculature map of (b) with $th = 0$. (d) The corresponding vasculature ground truth for (b) and (c), where (b)–(d) share the same scale bar. (e) The intensity profiles along the three white lines in (b). The light blue and red lines denote the ULM results and the ground truths, respectively. (f) The flow speed map of the leaf phantom in the same view as (a). (g) Magnification of the flow speed map within the red box in (f), corresponding to the same ROI in (b). (h) The flow speed profiles across three channels as indicated by the three white lines in (g). (i) Proportion of flow speed distribution in the flow speed map of the entire field of view in (f); the bin width is 2 mm s^{-1}; the red line represents the data fitted with a log-normal distribution.

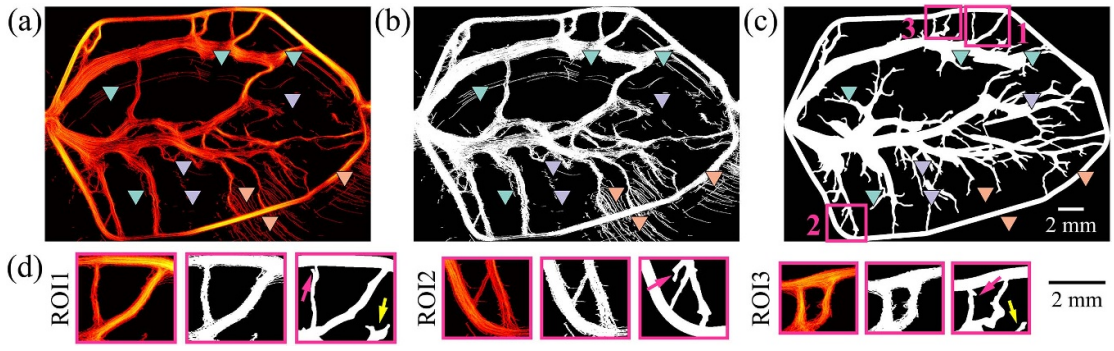

Figure 3. ULM of a kidney phantom: (a) The ULM density map of the kidney phantom. (b) Binarized vasculature map of (a) with the threshold (*th*) of 0. (c) The corresponding vasculature ground truth. (d) Side-by-side comparison of three zoomed-in ROIs enclosed by the magenta boxes in (c) across maps in (a)–(c). Note that (a)–(c) share the same scale bar.

4. Discussion

We introduced an on-chip versatile vasculature phantom protocol that enables flexible customization of micron-sized and hierarchical microvasculature. The phantom medium is agarose, which is both acoustically and optically transparent. Optical imaging provided more flow information for further assessment (supplementary videos 1–3), and the designed pattern in the AutoCAD file served as a structural ground truth. The minimum diameter of the fabricated channels was approximately 50 μm, far below the acoustic diffraction limit of most clinical and research-used ultrasound system settings. The success rate is high, over 90%, for the overall vasculature pattern transfer from a silicon wafer to an agarose-based microfluidic chip, while some defects may exist when the pattern is too complex with a channel

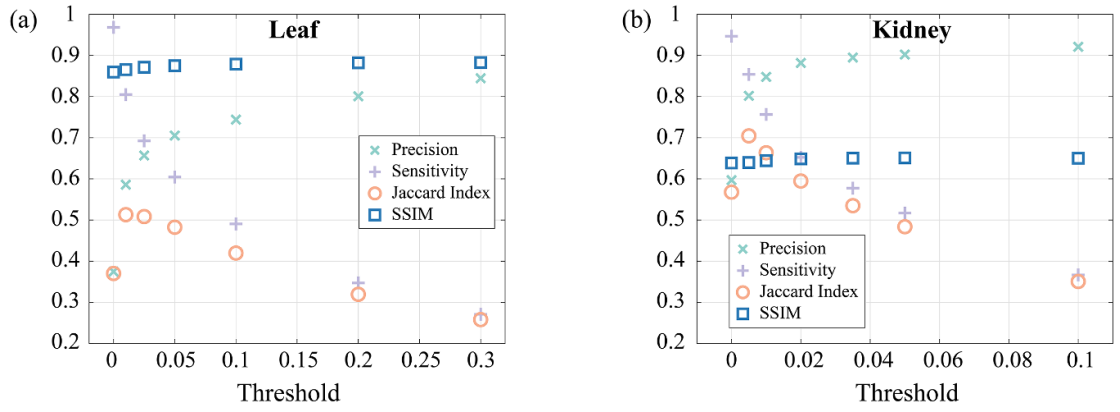

Figure 4. Quantitative analysis of ULM at different binarization thresholds for (a) the leaf and (b) the kidney phantoms based on the ROIs in figures 2(b) and 3(d), respectively.

diameter below 60 μm. The fabricated phantom can validate not only ULM but also other ultrasound and non-ultrasound microvascular imaging techniques.

ULM resolution was assessed using the leaf phantom, showing that ULM-estimated diameters of the microchannels (figure 2(e)) at half-maximum intensity were smaller than the ground truth values. This was because ULM relied on MB flow dynamics, and the MB signals extracted by SVD was related to the velocity distribution within the flow channel, resulting in a quasi-parabolic intensity profile (figure 2(e)). We observed positional deviations of some ULM-depicted channels from their ground truth positions (figure 2(e)). These shifts may have stemmed from misalignment during manual registration, pointed microchannels in the design, vessel broadening caused by ultrasound point spread function, and errors from localization and tracking methods in ULM. Such errors tend to accumulate throughout the ULM workflow, making positional shifts unavoidable. Future work should involve detailed evaluation using a simplified design of vasculatures.

The haemodynamic information obtained from ULM provides important functional insights. However, the pumpless perfusion of our current agarose-based microfluidic chip prevented us from obtaining ground truth velocity measurements. Nonetheless, the ULM-estimated flow speeds in the leaf phantom exhibited a log-normal distribution similar to that observed in *in vivo* vasculatures (Jafarnejad *et al* 2019, Yan *et al* 2024). This highlights the highly biomimetic nature of the proposed microvasculature phantom method.

For both leaf and kidney phantoms, the high sensitivity (0.97 and 0.95) but low precision (0.37 and 0.60) at $th = 0$ indicated that ULM successfully reconstructed the vessels within the selected ROIs but with a large number of FPs, particularly in the branching regions (figures 2(b) and 3(d)). As the binarization threshold increased, precision and JAC index increased while sensitivity decreased in both phantom cases. Yet, the kidney case had a higher precision than the leaf one. We attributed this observation to the microvasculature with fewer branches in the selected ROIs of the kidney case than that in the leaf case, which contained many branches. This finding highlighted the challenge for ULM to reconstruct branching structures more complex than straight channels.

The high visual correspondence between the ULM results and ground truth did not match the high FP rate. This discrepancy could be attributed to the intrinsic difference between the counting metric and SSIM. The metrics based solely on counting TP/FP/FN may have overlooked the overall vasculature and overemphasized the importance of each microbubble. Therefore, SSIM was used to measure the overall structural similarity between two images. The SSIM metrics for both the leaf and kidney phantoms were not impacted by different thresholds, indicating the integrity of the ULM-reconstructed microvascular networks. The lower SSIM observed for the kidney phantom might be due to its more irregular vascular network, such as pointed channels and small cul-de-sac regions (highlighted by the magenta arrows in figure 3(d)). The large spatial extent of FPs was multifactorial, involving misalignment during manual registration, vessel broadening from the ultrasonic point spread function, and localization and tracking errors in ULM. This evidenced the indispensability of a validation phantom for ULM to further improve the accuracy and robustness of the ULM workflow.

ULM could not reconstruct the lower half of the leaf vasculature in the image field of view, likely due to channel congestion caused by air. This may have resulted from high vascular complexity in that region, such as asymmetrical leaf venation and rich small branches, combined with the pumpless

nature of our hydrogel-based phantom. In this setup, the MB solution was perfused by capillary force and gravity. The pumpless perfusion stemmed from the inherent properties of agarose-based microfluidic chips, where the inlets cannot be effectively sealed when connected to a pump. Future studies may consider other hydrogel materials, like PEGDA (Polyethylene Glycol Diacrylate) and GelMA (Gelatin Methacrylate) for microfluidic chips (Bhusal *et al* 2021) that allow pump-driven perfusion. The kidney phantom had a more severe problem with air congestion (the purple triangles in figure 3 and supplementary video 2) because of its much more complex vasculature, including multiscale microvascular network and more bifurcations, than that in the leaf phantom. The kidney vasculature map reconstructed by ULM generally agreed with the ground truth image, but its quality was multifactorial. The cul-de-sac channels, marked by the turquoise triangles in figure 3 and shown in the supplementary video 1, had no circulatory flow so that ULM failed to detect them. Since the agarose microfluidic chip was sealed spontaneously by hydrogen bonds, the adhesion could not be guaranteed as reliably as that of traditional PDMS-based microfluidic chips. In our experiments, fluid leakage occurred in the areas that were indicated by the orange triangles in figure 3 and supplementary video 3, where free MB trajectories were delineated by ULM. It is important to note that the issue of fluid leakage could be mitigated through proper pattern design, such as avoiding cul-de-sac channels. This may explain why there was no fluid leakage observed in the leaf phantom. Computational modeling could serve as a valuable approach to design vasculature and validate perfusion feasibility prior to fabrication.

Manual spatial registration between the ULM and ground truth images may have led to alignment errors although the high sensitivity at $th = 0$ indicated good registration. In particular, the channel depth of our phantoms was 240 μm, which was deemed to be relatively large for a typical microfluidic chip. The large channel depth was designed to facilitate pumpless perfusion but might cause photolithography defects. Moreover, generation of the ULM images involved many parameters in the localization and tracking steps, including SVD cut-off threshold, the number of MBs per frame, localization methods, the minimum trajectory length, and so on. Finding the optimal set of parameters is an exhaustive task. The parameters that were used for the leaf and kidney data in this study were summarized in table S1 of the supplementary material.

Overall, the proposed on-chip vasculature protocol provides a valuable method to validate and assess the performance of ULM, showing significant potential for the development and optimization of ultrasound microvascular imaging techniques. The methodology also paves the way for developing versatile organ-on-a-chip devices. Future work could focus on performance evaluation of volumetric ULM and micro-Doppler imaging with flow velocity information.

Data availability statement

The data that support the findings of this study are openly available at the following URL/DOI: https://doi.org/10.5281/zenodo.15614916. Data will be available from 01 December 2025.

ULM parameters available at https://doi.org/10.1088/1361-6560/ae11f6/data1.

No circulatory flow in the chip available at https://doi.org/10.1088/1361-6560/ae11f6/data2.

Air congestion in the chip available at https://doi.org/10.1088/1361-6560/ae11f6/data3.

Fluid leakage in the chip available at https://doi.org/10.1088/1361-6560/ae11f6/data4.

Acknowledgment

Renxian Wang is supported by ACCESS—AI Chip Center for Emerging Smart Systems, sponsored by the InnoHK initiative of the Innovation and Technology Commission of the Hong Kong Special Administrative Region Government. This work was in part supported by Collaborative Research with World-leading Research Groups from The Hong Kong Polytechnic University (P0039523) and Hong Kong Research Grants Council Theme-based Research Scheme (T46-705/23-R).

ORCID iDs

Renxian Wang 0000-0003-3357-218X
Xin Zhao 0000-0002-9521-7768
Wei-Ning Lee 0000-0001-8799-2492

References

Andersen S B, Taghavi I, Kjer H M, Sogaard S B, Gundlach C, Dahl V A, Nielsen M B, Dahl A B, Jensen J A and Sorensen C M 2021 Evaluation of 2D super-resolution ultrasound imaging of the rat renal vasculature using *ex vivo* micro-computed tomography *Sci. Rep.* **11** 24335

Bhusal A, Dogan E, Nguyen H A, Labutina O, Nieto D, Khademhosseini A and Miri A K 2021 Multi-material digital light processing bioprinting of hydrogel-based microfluidic chips *Biofabrication* **14** 014103

Blanken N, Heiles B, Kuliesh A, Versuis M, Jain K, Maresca D and Lajoinie G 2024 PROTEUS: a physically realistic contrast-enhanced ultrasound simulator-part I: numerical methods *IEEE Trans. Ultrason. Ferroelectr. Freq. Control* **72** 848–65

Chabouh G, Denis L, Bodard S, Lager F, Renault G, Chavignon A and Couture O 2024 Whole organ volumetric sensing ultrasound localization microscopy for characterization of kidney structure *IEEE Trans. Med. Imaging* **43** 4055–63

Chen X, Lowerison M R, Dong Z, Chandra Sekaran N V, Llano D A and Song P 2023 Localization free super-resolution microbubble velocimetry using a long short-term memory neural network *IEEE Trans. Med. Imaging* **42** 2374–85

Christensen-Jeffries K *et al* 2020 Super-resolution ultrasound imaging *Ultrasound Med. Biol.* **46** 865–91

Demene C, Robin J, Dizeux A, Heiles B, Pernot M, Tanter M and Perren F 2021 Transcranial ultrafast ultrasound localization microscopy of brain vasculature in patients *Nat. Biomed. Eng.* **5** 219–28

Errico C, Pierre J, Pezet S, Desailly Y, Lenkei Z, Couture O and Tanter M 2015 Ultrafast ultrasound localization microscopy for deep super-resolution vascular imaging *Nature* **527** 499–502

Fang J, Liu H, Qiao W, Xu T, Yang Y, Xie H, Lam C H, Yeung K W K and Zhao X 2023 Biomimicking leaf-vein engraved soft and elastic membrane promotes vascular reconstruction *Adv. Healthcare Mater.* **12** e2201220

Gershman Y, Shapiro G, Mano T and Ilovitsh T 2025 Flow analysis in pathological microvascular models by ultrasound localization microscopy *Adv. Mater. Technol.* **10** e02208

Hansen L N, Ráth A, Amin Naji M, McDermott A, Sørensen C M, Kjer H M, Gundlach C, Dahl A B and Jensen J A 2025 Assessment of super-resolution ultrasound imaging using the erythrocytes through comparison with micro-CT *Proc. SPIE 13412, Medical Imaging 2025: Ultrasonic Imaging and Tomography* (vol 1341203) (https://doi.org/10.1117/12.3046511)

Heiles B, Chavignon A, Hingot V, Lopez P, Teston E and Couture O 2022 Performance benchmarking of microbubble-localization algorithms for ultrasound localization microscopy *Nat. Biomed. Eng.* **6** 605–16

Jafarnejad M, Ismail A Z, Duarte D, Vyas C, Ghahramani A, Zawieja D C, Lo Celso C, Poologasundarampillai G and Moore J E Jr 2019 Quantification of the whole lymph node vasculature based on tomography of the vessel corrosion casts *Sci. Rep.* **9** 13380

Ji X, Bei H P, Zhong G, Shao H, He X, Qian X, Zhang Y and Zhao X 2023 Premetastatic niche mimicking bone-on-a-chip: a microfluidic platform to study bone metastasis in cancer patients *Small* **19** 2207606

Kawara S, Cunningham B, Bezer J, Kc N, Zhu J, Tang M X, Ishihara J, Choi J J and Au S H 2023 Capillary-scale hydrogel microchannel networks by wire templating *Small* **19** 1–10

Kuhn H W 1955 The Hungarian method for the assignment problem *Nav. Res. Logist. Q.* **2** 83–97

Lerendegui M *et al* 2024 ULTRA-SR challenge: assessment of ultrasound localization and tracking algorithms for super-resolution imaging *IEEE Trans. Med. Imaging* **43** 2970–87

Li L, Hu W, Lu J and Zhang C 2022 Leaf vein segmentation with self-supervision *Comput. Electron. Agric.* **203** 107352

Lowerison M R, Sekaran N V C, Zhang W, Dong Z, Chen X, Llano D A and Song P 2022 Aging-related cerebral microvascular changes visualized using ultrasound localization microscopy in the living mouse *Sci. Rep.* **12** 619

Mano T, Grutman T and Ilovitsh T 2023 Versatile ultrasound-compatible microfluidic platform for *in vitro* microvasculature flow research and imaging optimization *ACS Omega* **8** 47667–77

Mao M, Bei H P, Lam C H, Chen P, Wang S, Chen Y, He J and Zhao X 2020 Human-on-leaf-chip: a biomimetic vascular system integrated with chamber-specific organs *Small* **16** e2000546

Mao M, He J, Lu Y, Li X, Li T, Zhou W and Li D 2018 Leaf-templated, microwell-integrated microfluidic chips for high-throughput cell experiments *Biofabrication* **10** 025008

Parra Raad J, Lock D, Liu Y Y, Solomon M, Peralta L and Christensen-Jeffries K 2024 Optically validated microvascular phantom for super-resolution ultrasound imaging *IEEE Trans. Ultrason. Ferroelectr. Freq. Control* **71** 1833–43

Riemer K, Toulemonde M, Yan J, Lerendegui M, Stride E, Weinberg P D, Dunsby C and Tang M X 2023 Fast and selective super-resolution ultrasound *in vivo* with acoustically activated nanodroplets *IEEE Trans. Med. Imaging* **42** 1056–67

Song P, Trzasko J D, Manduca A, Huang R, Kadirvel R, Kallmes D F and Chen S 2018 Improved super-resolution ultrasound microvessel imaging with spatiotemporal nonlocal means filtering and bipartite graph-based microbubble tracking *IEEE Trans. Ultrason. Ferroelectr. Freq. Control* **65** 149–67

Walsh C L *et al* 2021 Imaging intact human organs with local resolution of cellular structures using hierarchical phase-contrast tomography *Nat. Methods* **18** 1532–41

Wang B, Riemer K, Toulemonde M, Yan J, Zhou X, Smith C A B and Tang M X 2024 Broad elevation projection super-resolution ultrasound (BEP-SRUS) imaging with a 1-D unfocused linear array *IEEE Trans. Ultrason. Ferroelectr. Freq. Control* **71** 255–65

Wang Z, Bovik C A, Sheikh R H and Simoncelli P E 2004 Image quality assessment: from error visibility to structural similarity *IEEE Trans. Image Process* **13** 600–12

Yan J *et al* 2024 Transthoracic ultrasound localization microscopy of myocardial vasculature in patients *Nat. Biomed. Eng.* **8** 689–700

Yan J, Zhang T, Broughton-Venner J, Huang P and Tang M X 2022 Super-resolution ultrasound through sparsity-based deconvolution and multi-feature tracking *IEEE Trans. Med. Imaging* **41** 1938–47

Zhang G, Harput S, Hu H, Christensen-Jeffries K, Zhu J, Brown J, Leow C H, Eckersley R J, Dunsby C and Tang M X 2019 Fast acoustic wave sparsely activated localization microscopy (fast-AWSALM): ultrasound super-resolution using plane-wave activation of nanodroplets *IEEE Trans. Ultrason. Ferroelectr. Freq. Control* **66** 1039–46